ACS OMEGA

Open Access

http://pubs.acs.org/journal/acsodf

Article

Discovery of Chemical Scaffolds as Lysophosphatidic Acid Receptor 1 Antagonists: Virtual Screening, *In Vitro* Validation, and Molecular Dynamics Analysis

Lan Phuong Nguyen, Rasel Ahmed Khan, Soomin Kang, Hobin Lee, Jong-Ik Hwang,* and Hong-Rae Kim*

Cite This: *ACS Omega* 2023, 8, 40375−40386

Read Online

ACCESS | Metrics & More | Article Recommendations | Supporting Information

ABSTRACT: Lysophosphatidic acid receptor 1 (LPAR1) is an emerging therapeutic target for numerous human diseases including fibrosis. However, the limited number of available core structures of LPAR1 antagonists has prompted the need for novel chemical templates. In this study, we conducted a high-throughput virtual screening to discover potential new scaffolds. We tested three existing crystal structures alongside an AlphaFold model to evaluate their suitability in structure-based virtual screening, finding that the crystal structures show superior performance compared with the predictive model. Furthermore, we also found that enhancing the precision in the screening process did not necessarily improve the enrichment of hits. From the screening campaign, we identified five structures that were validated using an LPAR1-dependent calcium flux assay. To gain a deeper insight into the protein−ligand interaction, we extensively analyzed the binding modes of these compounds using *in silico* techniques, laying the groundwork for the discovery of novel LPAR1 antagonists.

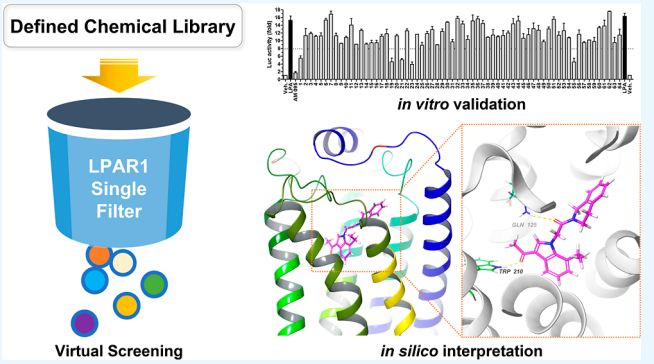

1. INTRODUCTION

Lysophosphatidic acid (LPA) is a bioactive phospholipid signaling molecule that interacts with and activates lysophosphatidic acid receptors (LPARs), a family of G protein-coupled receptors. Due to its involvement in various physiological processes,[1] the LPA−LPAR signaling pathway has been implicated in numerous human diseases.[2,3] Among the six identified LPA receptors, LPAR1 has been particularly highlighted due to its central involvement in fibrotic diseases.[4,5] Clinical studies have found elevated levels of LPA and increased expression of LPAR1 in patients with idiopathic pulmonary fibrosis (IPF).[6] Experimental evidence further supports the role of LPAR1 in IPF, as protection against the disease has been observed in a bleomycin-induced lung fibrosis model using LPA1-null mice.[7] The encouraging results from recent phase II clinical trials using BMS-986278,[8] a potent and selective LPAR1 antagonist, have underscored LPAR1 as a viable therapeutic target for IPF. Moreover, emerging studies are exploring the importance of LPAR1 in the central nervous system,[9] suggesting further potential for therapeutic applications.

While several LPAR1 antagonists, including BMS-96278,[10] BMS-986020,[11] Ki16425,[12] ONO-730043,[13] and SAR-100842[14] (Figure 1), have been identified to date, their structural similarities, as discussed in a recent review article,[15] highlight the need for expanding the available repertoire of chemical templates capable of inducing LPAR1 antagonism. The importance of this diversification is underscored by BMS-986020's hepatobiliary toxicity, which was found to be structure-dependent, a contrast to antagonists with distinct structural features that did not exhibit this toxicity.[16] By diversification of the chemical space, valuable insights into protein−ligand interactions can be gained, potentially leading to the discovery of novel candidates with improved pharmacological profiles, devoid of toxicity associated with certain structural elements.

To address this need, we conducted a high-throughput virtual screening campaign with the primary goal of identifying novel chemical scaffolds possessing LPAR1 antagonistic activity. By employing structure-based virtual screening, we carefully selected a protein template for screening and subsequently validated the obtained results using an LPAR1-dependent calcium flux assay. To gain deeper insights into the molecular interactions and dynamics, we further performed

Received: July 4, 2023
Accepted: October 6, 2023
Published: October 18, 2023

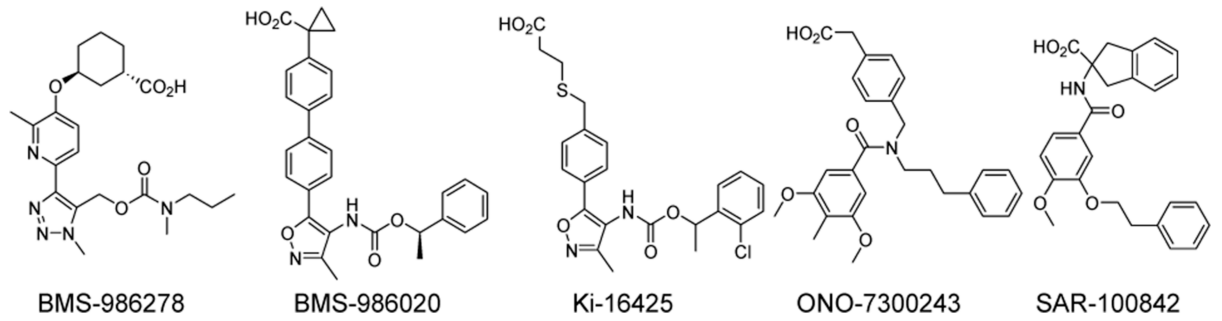

Figure 1. Representative LPAR1 antagonists.

molecular dynamics simulations to interpret our findings. Collectively, these efforts establish a foundation for the exploration and development of novel LPAR1 antagonists with potential therapeutic applications.

2. RESULTS AND DISCUSSION

2.1. Evaluation of Protein Structures for Structure-Based Virtual Screening. The success of structure-based virtual screening heavily relies on careful selection of an appropriate protein template for the screening process. In this study, we evaluated three crystal structures of LPAR1 (PDB IDs: 4Z34, 4Z35, and 4Z36)[17] known to date, all of which are ligand-bound *holo* structures, to determine the template with the highest potential for identifying novel chemical entities. While *holo* structures are generally known to exhibit better performance in virtual screening campaigns,[18] we also included an AlphaFold model as an *apo-like* structure[19] for comparison. A comparative analysis was conducted to evaluate the performance of each structure in distinguishing known inhibitors (answer set) from DUD-E generated decoys,[20] with the aim of identifying the most effective template.

We selected 10 experimentally validated antagonists from the literature (Table S1) and generated 50 decoys for each, resulting in a total of 510 compounds for performance evaluation. To account for variations in the protonation states and isomers, we generated all possible molecular forms of the 510 compounds at a target pH of 7.0 ± 2.0, resulting in a set of 1161 unique chemical entities. After each round of screening, we selected the most plausible state for each compound, progressively refining the data set.

For the evaluation, we utilized Schrodinger's built-in virtual screening workflow (VSW), powered by Glide.[21] The VSW consisted of three successive screening steps: high-throughput virtual screening (HTVS), standard precision (SP) screening, and extra precision (XP)[22] screening. The top 10% of compounds from the HTVS screening were selected for the SP screening, and subsequently, the top 10% from the SP screening underwent the XP screening. The evaluation was based on the five compounds with the highest ranking in the final XP screening.

Within the VSW, structures 4Z34 and 4Z36 successfully identified SAR-100842 as one of the top five compounds (Table S2). However, neither structure 4Z35 nor the AlphaFold model managed to retrieve any of the true binders. Notably, none of the structures were able to identify the other antagonists in the top five compounds through the VSW screening process.

To gain a more comprehensive understanding of the results, we conducted a manual evaluation of each step in the VSW and analyzed its performance (Table 1). During the HTVS screening, 4Z35 exhibited the highest enrichment with a

Table 1. Performance Evaluation of Each Protein Structure with Respect to Precision of the Docking Process

precision[a]	PDB	BEDROC[b] (α = 160.9)	BEDROC[b] (α = 8.0)	AUAUC[c]	$EF_{1\%}$[d]
HTVS	AlphaFold[e]	0.005	0.261	0.64	0
	4Z34	0.118	0.356	0.60	10
	4Z35	0.266	0.429	0.70	10
	4Z36	0.152	0.300	0.59	10
SP	AlphaFold[e]	0.000	0.201	0.61	0
	4Z34	0.601	0.604	0.89	31
	4Z35	0.365	0.462	0.82	20
	4Z36	0.366	0.461	0.79	20
XP	AlphaFold[e]	0.000	0.070	0.37	0
	4Z34	0.615	0.567	0.79	31
	4Z35	0.283	0.238	0.63	10
	4Z36	0.128	0.295	0.55	10

[a]Thoroughness of the docking process. HTVS: high-throughput virtual screening; SP: standard precision; XP: extra precision. [b]BEDROC: Boltzmann-enhanced discrimination of receiver operating characteristic. [c]AUAUC: area under the accumulation curve. [d]$EF_{1\%}$: enrichment factor 1%. [e]AlphaFold: AF-Q92633-F1-model_v4 was used.

BEDROC[23] (α = 160.9) value of 0.266; however, none of the four protein structures successfully recognized ONO-9780307 as a true binder. This implies that the ONO-9780307 was eliminated in the initial round of the VSW, impeding its retrieval in subsequent screening processes.

Interestingly, screening with a higher precision did not correlate with improved enrichment. In the case of structure 4Z34, a significant enhancement in enrichment was observed from HTVS to standard precision (SP), but further refinement to XP settings led to only a minimal increase in the BEDROC value (α = 160.9), coupled with a decrease in both BEDROC (α = 8.0) and AUAUC values. This occurred despite the cost of extended computing time, resulting in no improvement in $EF_{1\%}$. For structures 4Z35 and 4Z36, enrichment values for SP screening outperformed those of XP in all four metrics, showing no correlation between the precision and enrichment. Disappointingly, irrespective of the precision of screening, the AlphaFold model showed poor enrichment in terms of the BEDROC (α = 160.9) value.

Overall, the most successful performance was observed with the 4Z34 XP setting. However, the improvement over SP screening was marginal, especially considering the extensive computing resources required. Recognizing that the majority of

https://doi.org/10.1021/acsomega.3c04798
ACS Omega 2023, 8, 40375−40386

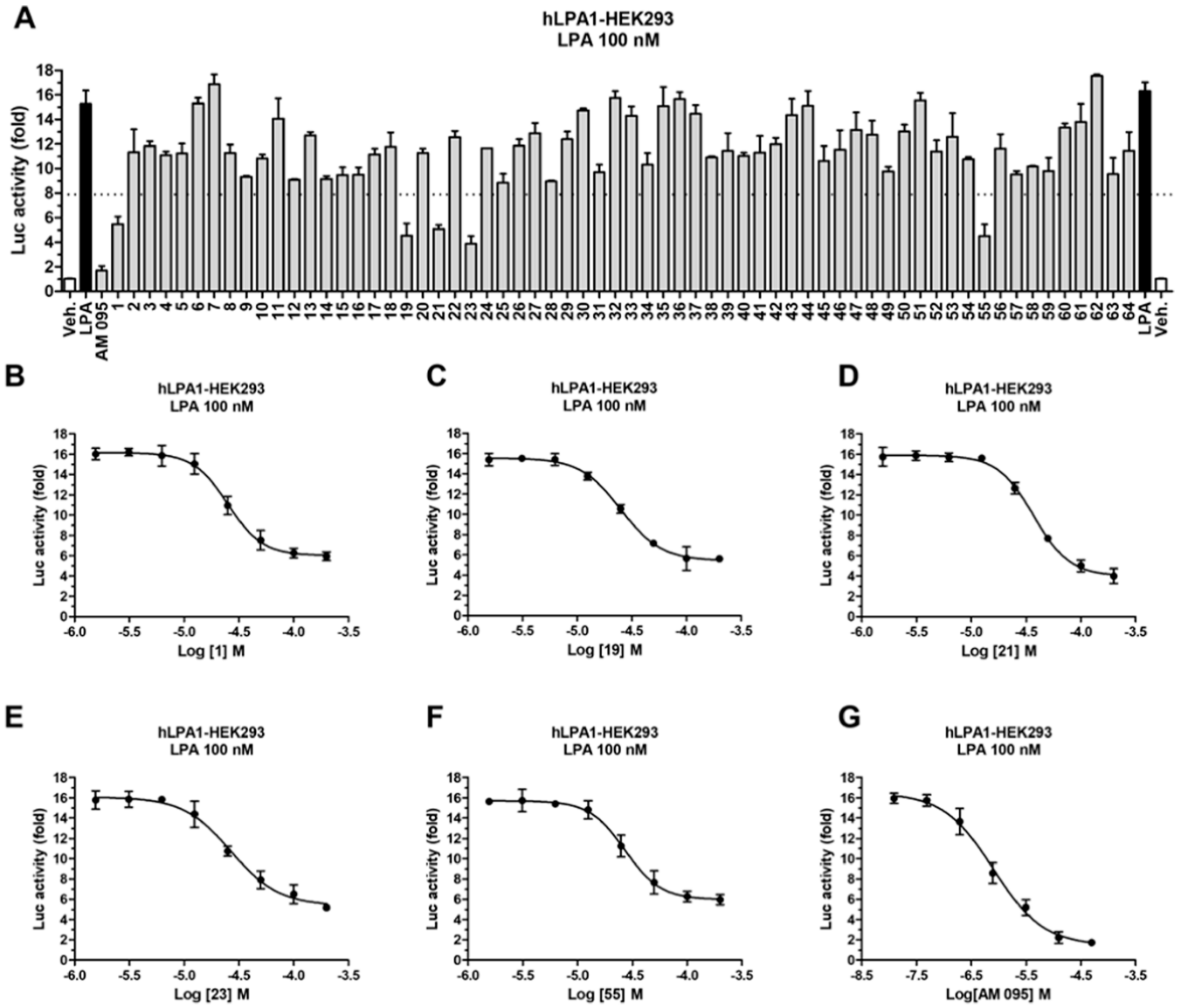

Figure 2. LPAR1-dependent calcium flux assay. (A) Inhibitory activity of compounds derived from virtual screening. Compounds were pretreated with a fixed concentration of 50 μM. Dose-dependent activity of compounds (B) 1, (C) 19, (D) 21, (E) 23, (F) 55, and (G) AM095 as a positive control.

the actives were being lost during the initial HTVS screening process, we opted to focus our screening entirely on 4Z34 with SP settings rather than employing multiple layers of varying precisions to narrow down the number of compounds being screened.

2.2. High-Throughput Virtual Screening and Selection of Compounds for *in Vitro* Validation. In our pursuit of the identification of novel scaffolds, we prioritized virtual compound libraries with structural diversity and commercial availability. The growing size of virtual libraries has led to debates on whether screening larger libraries can improve the chances of discovering more promising hit compounds;[24] however, the significance of screening a larger chemical space is influenced by various factors and remains an ongoing topic.[25] Taking into account the computational resources required to screen the entire library with standard precision (SP), we decided to screen the ChemBridge DIVERSet. This library encompasses 1.3 million readily available compounds, which is a manageable size, and offers a wide range of structural diversity.

Following the SP precision screening of the complete library, we selected the top 200 compounds based on the docking score. These compounds were further subjected to clustering based on structural similarity and underwent additional filters, including drug-likeness and visual inspection. Ultimately, a total of 64 compounds (Table S3) were chosen for *in vitro* validation.

In order to measure the inhibitory activity of the derived compounds, we conducted an LPAR1-dependent calcium flux assay, utilizing AM095 as a positive control. Intracellular calcium increase was measured upon pretreatment of compounds (50 μM) at 37 °C for 20 min, followed by 10 min at room temperature to stabilize the cells. From the assay, we identified five distinct chemical structures that exhibited greater than 50% inhibition in the LPAR1-dependent calcium flux assay (Figure 2A). These compounds were retested with varying concentrations (eight-point twofold dilutions starting

https://doi.org/10.1021/acsomega.3c04798
ACS Omega 2023, 8, 40375−40386

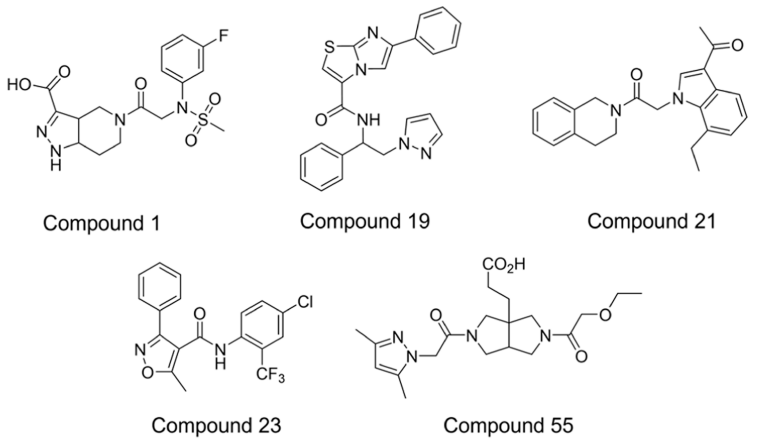

Compound	M.W.[a]	Docking Score	MM-GBSA[b]	IC_{50} (μM)
1	396	-9.018	-40.52	25.089 ± 2.738
19	413	-8.567	-44.01	25.048 ± 2.406
21	360	-7.976	-52.16	37.004 ± 2.974
23	381	-8.561	-51.86	26.839 ± 4.308
55	406	-7.869	-46.71	27.147 ± 3.357
AM095	457	-7.254	-63.62	0.805 ± 0.208

Figure 3. Structures and properties of top 5 compounds derived from the virtual screening and AM095. [a]M.W.: molecular weight. [b]MM-GBSA: molecular mechanics with generalized Born and surface area solvation.

from 200 μM), confirming a dose-dependent behavior (Figure 2B−F).

The measured IC_{50} indicated that the five compounds derived from the virtual screening campaign are weak inhibitors of LPAR1 (Figure 3). However, all the identified compounds have lead-like structures with molecular weights ranging from 381 to 413, and an acceptable range of log *P* and the number of hydrogen bonding donors/acceptors (Table S4). A thorough study for understanding how these compounds bind would provide insights into designing novel structures with improved properties; hence, we investigated each compound's binding mode through *in silico* methods.

2.3. Scaffolds Containing Carboxylic Acids. The majority of the LPAR1 antagonists reported to date contain a carboxylic acid moiety, which is believed to be involved in interactions with polar and ionic residues located toward the N-terminal capping helix, specifically His40, Lys39, and Tyr34.[17] The molecular docking studies of compound 1 with LPAR1 (Figure 4A,B) revealed that the ligand's carboxylate group interacts with Arg124, Lys39, and Tyr34, as anticipated. Another significant interaction identified was the hydrogen bonding between the carbonyl group and Gln125. In a 100 ns molecular dynamics simulation, the system reached equilibration, with an average ligand RMSD value of 2.458 Å with respect to the protein. Interestingly, while the molecular docking analysis identified Arg124 and Lys39 interacting with the carboxylate, the molecular dynamics simulation showed that the dominant interaction is with Arg124. The hydrogen bonding interaction between the carbonyl group and Gln125 was the second most frequently observed interaction. Notably, the molecular docking studies did not identify the hydrogen bonding interaction between the amino group of indazole and Glu293, as well as the hydrogen bonding interaction between the sulfonyl oxygen and Trp210, both of which were observed in the molecular dynamics simulation (Figure S2).

In the case of compound 55, as evidenced by molecular docking studies (Figure 4E,F), the carboxylate group interacted with Arg124, Lys39, and Tyr34, along with an additional interaction with His40. Previous studies have suggested that His40 may play a crucial role in the selectivity profile as it is unique to LPAR1.[17] The molecular dynamics analysis supported that these interactions were the primary contributing factors in binding (Figure 4H). The overall system reached equilibration toward the end of the simulation, possibly due to the presence of a high number of rotatable bonds (Figure 4G). Apart from the carboxylate moiety, both carbonyl groups of the amides actively participated in the binding process. A hydrogen bonding interaction of amide carbonyl with Gln125 was again observed; however, a unique water bridge was present between Thr109 and the remaining amide carbonyl of compound 55. Considering the potential for structural modifications, this unique fused bicyclic core may present a promising template worthy of further investigation.

2.4. Compound 21 Mimics the Binding of ONO-9910539. Compound 21, identified through the molecular docking analysis, exhibited two significant hydrogen bonding interactions: (1) Trp210 with the acetyl carbonyl group and (2) Gln125 with the amide carbonyl group (Figure 5A,B). These hydrogen bonding interactions remained dominant during a 100 ns MD simulation (Figure 5D), emphasizing their importance. Compound 21 displayed minimal deviation of the ligand from the initially predicted position, with an average RMSD of 1.351 Å (Figure 5C), which was the lowest RMSD value observed among all of the simulated compounds.

Interestingly, despite its structural difference, compound 21 demonstrated an identical interaction pattern to ONO-9910539, as observed in the analysis of ONO-9910539 bound to LPAR1 (PDB: 4Z35).

The available crystal structures of LPAR1 are all *holo* structures in complex with a series of analogues (ONO-

https://doi.org/10.1021/acsomega.3c04798
ACS Omega 2023, 8, 40375−40386

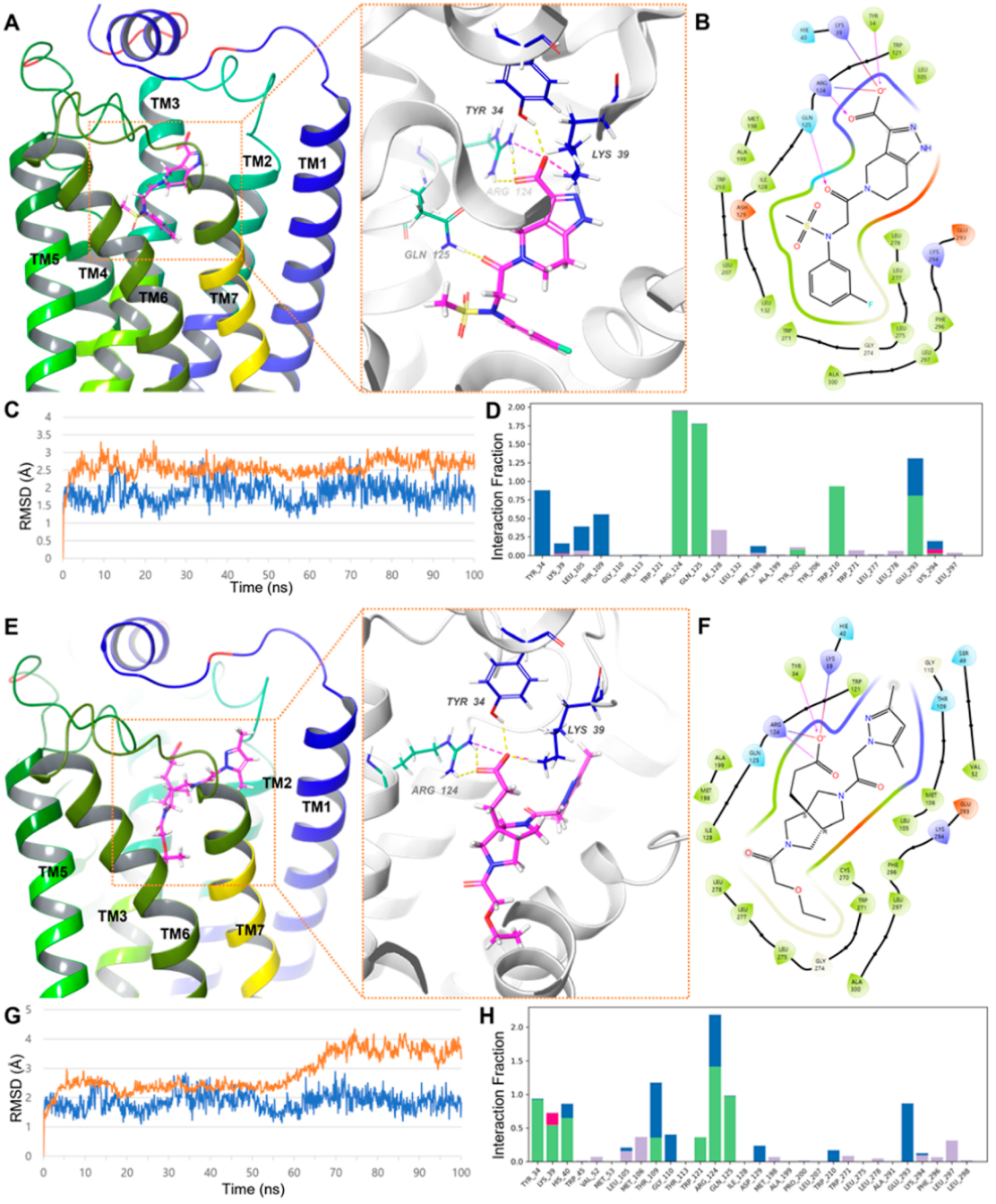

Figure 4. Protein−ligand interaction analysis of compounds with a carboxylic acid moiety. (A,E) Binding pose prediction and (B,F) protein−ligand interaction of compounds 1 and 55, respectively, determined by molecular docking studies. The yellow dashed line indicates hydrogen bonding, and the purple dashed line indicates salt bridges in the orange box. The arrows in the protein−ligand interaction diagram indicates hydrogen bonding interactions, and the purple solid line indicates salt bridges. (C,G) RMSD plot of protein (orange) and ligand (blue), and (D,H) frequency of interacting residues observed over the course of 100 ns molecular dynamics simulation for compounds 1 and 55, respectively. For the interaction fraction diagram, green indicates hydrogen bonding interactions, purple indicates hydrophobic interactions including $\pi-\pi$ and $\pi-$cation interactions, blue indicates water bridges, and magenta indicates ionic interactions.

9780307, 9910539, and 3080573) containing a common chiral secondary hydroxyl moiety (Figure S3). While the crystal structures 4Z34 and 4Z36 displayed a hydrogen bonding interaction between these hydroxyl groups and the side chain of Gln125, this interaction was not observed in 4Z35, neither in the crystal structure nor in the molecular docking analysis. A possible explanation for this discrepancy may be attributed to the crystal structure being only a "snapshot" of a dynamic interaction. Indeed, a 100 ns molecular dynamics simulation identified the hydrogen bonding interaction between this hydroxyl group and the side chain of Gln125, similar to the observed interaction in the other two structures (Figures 6A and S4). ONO-9910539, the only analogue of the methyl ketone moiety, ONO-9910539, exhibited an identical hydrogen bonding interaction between the carbonyl group with Trp210.

Overlaying the crystal structure of ONO-9910539 with the docked pose of compound 21 demonstrated alignment of the

https://doi.org/10.1021/acsomega.3c04798
ACS Omega 2023, 8, 40375−40386

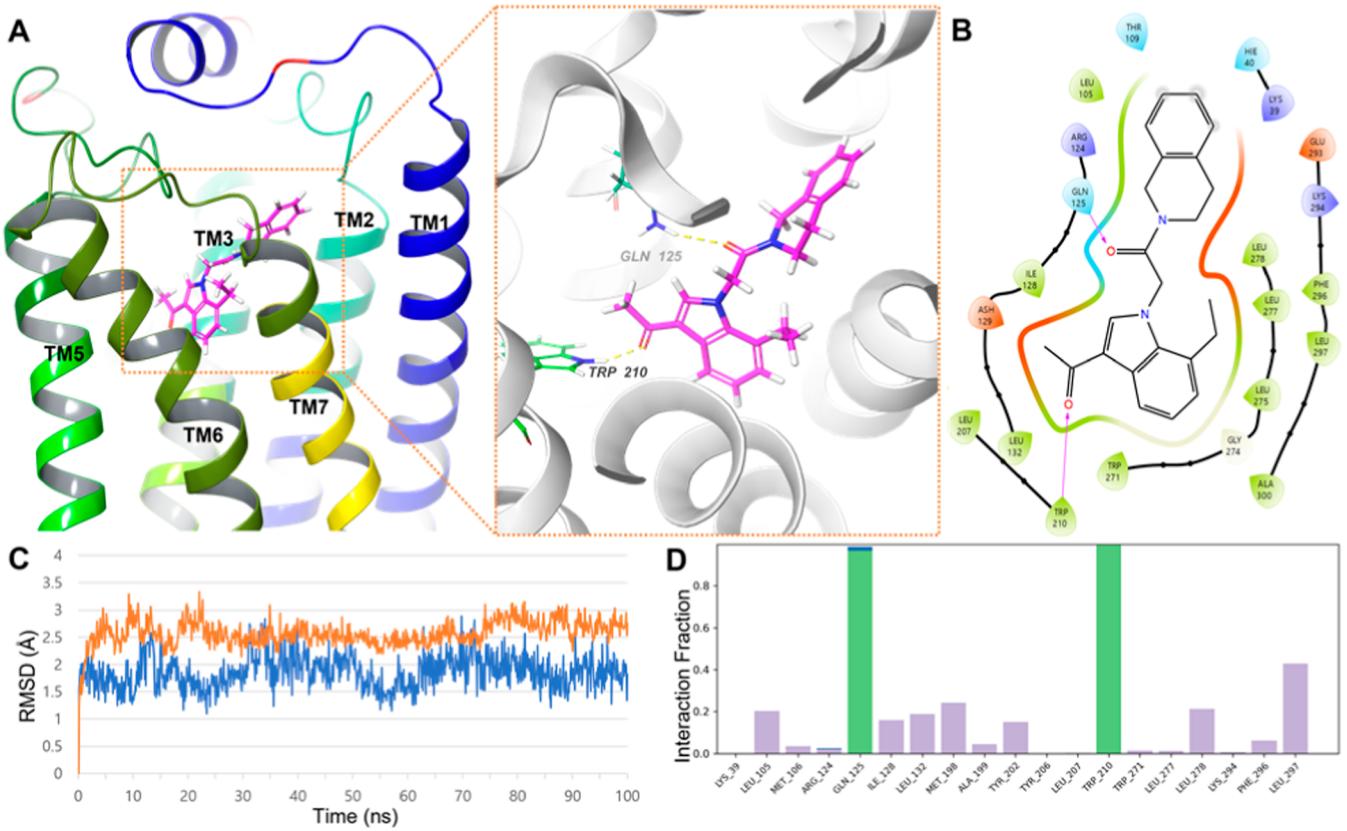

Figure 5. Protein−ligand interaction analysis of compound 21. (A) Binding pose prediction and (B) protein−ligand interaction determined by molecular docking studies. The yellow dashed line indicates hydrogen bonding, and the purple dashed line indicates salt bridges in the orange box. The arrow in (B) indicates hydrogen bonding interactions. (C) RMSD plot of protein (orange) and ligand (blue) and (D) Frequency of interacting residues observed over the course of 100 ns molecular dynamics simulation. For (D), green indicates hydrogen bonding interactions, and purple indicates hydrophobic interactions including $\pi-\pi$ and $\pi-$cation interactions.

methyl ketones, along with the two ring systems, in a 3D pharmacology hypothesis model (Figure 6B). The key difference between the two compounds lies in the mode of hydrogen bonding: the hydroxyl group of the ONO compounds acting as a hydrogen bond donor to the carbonyl group of the Gln125 side chain, whereas in compound 21, the carbonyl group of the ligand served as the hydrogen bond acceptor, while the amino group of the Gln125 side chain became the hydrogen bond donor (Figure 6D). This analysis indicates that the two structural motifs could be in a bioisoteric relationship.

2.5. Imidazolothiazole and Isoxazole Scaffolds. The molecular docking analysis of compound 19 revealed a hydrogen bonding interaction between the amide carbonyl group and Gln125 of LPAR1, which was identified as the key interaction (Figure 7A,B). However, during a 100 ns molecular dynamics simulation, a hydrophobic $\pi-\pi$ stacking interaction between Trp271 of LPAR1 and the pyrazole moiety of the ligand was found to be the most frequently observed interaction (Figure 7H). This interaction was further stabilized by a water bridge formed between Arg124 and N7 of the imidazolothiazole moiety. *In silico* analysis indicated that the (*S*)-configuration of the compound is the more active isomer, as the (*R*)-enantiomer did not show promising results during the virtual screening process. The system reached equilibration during the simulation, with an overall average RMSD of 1.978 Å for the ligand with respect to the protein (Figure 7C).

Compound 23 was initially expected to have a binding mode similar to that of BMS-986020 or Ki16425, given its structural resemblance to these antagonists. However, contrary to expectations, compound 23 displayed an opposite binding orientation compared to BMS-986020 or Ki16425 (Figure 7E,F). Although there is no crystal structure of BMS-986020 or Ki16425 bound to LPAR1 reported to date, previous studies suggest that the carboxylic acid moiety of these antagonists engages in ionic interactions with residues located toward the N-terminus, such as Lys39 and His40, which play a crucial role.[17] As a result, the carbamate moiety of these reported antagonists is expected to be positioned deeper toward the membrane, as confirmed by molecular docking experiments (Figure S5). It should be noted that depending on the installation of additional substituents at either side of the ring, the orientation could possibly flip to adopt the orientation of BMS-986020 or its analogues. However, at the same time, fine-tuning of either side of the rings could potentially fix the proposed binding pose and possibly be beneficial in binding through interactions with Gln125.

3. DISCUSSION

In this study, we employed a comprehensive virtual screening approach to identify novel scaffolds as LPAR1 antagonists. Our findings provided valuable insights and highlighted several important observations. First and foremost, in line with numerous preceding studies,[26,27] the docking scores did not consistently correlate with inhibitor activity. Interestingly,

https://doi.org/10.1021/acsomega.3c04798
ACS Omega 2023, 8, 40375−40386

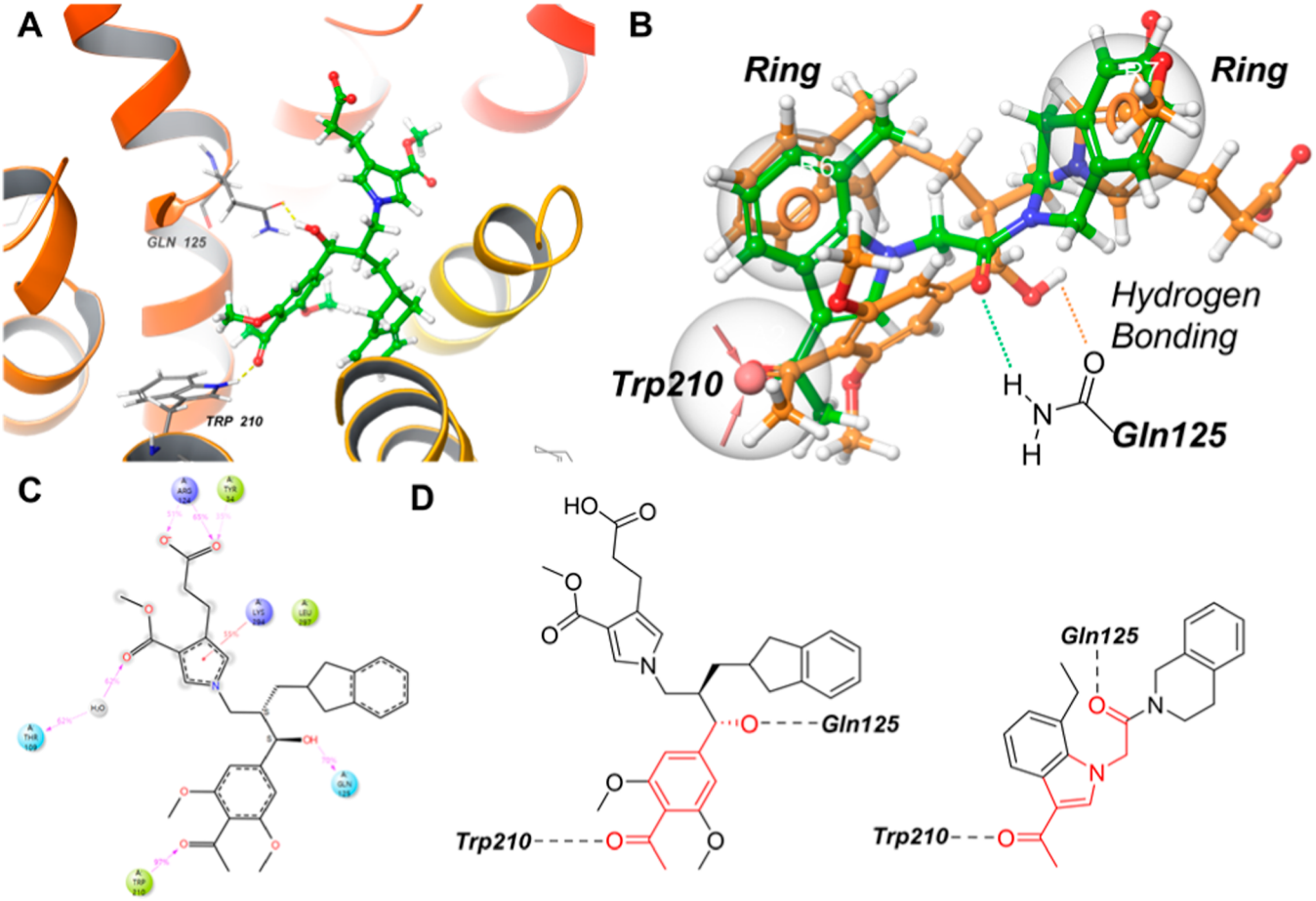

Figure 6. Binding mode comparison of ONO-9910539 and compound 21. (A) Snapshot of ONO-9910539 interacting with LPAR during a course of 100 ns MD simulation. Hydrogen bonding is indicated in yellow. (B) 3D pharmacophore modeling of the two ligands. ONO-9910539, taken from the crystal structure 4Z35, is depicted in orange, and the predicted docking pose of compound 21 is depicted in green. (C) Protein−ligand interaction of ONO-9910539 over a course of 100 ns molecular dynamics simulation. (D) Structural comparison between the two compounds. The colored structure indicates a possible bioisosteric relationship.

when plotting docking scores against percent inhibition at 50 μM, we found no correlation across the full population (Figure 8A) but rather identified an inverse relationship within the active compounds (Figure 8B). Conversely, comparing MM-GBSA values with the percent inhibition of the actives did reveal some degree of correlation (Figure 8C,D). However, a larger sample size would be necessary to arrive at definitive conclusions. Furthermore, we observed that crystal structures in their holo form outperformed the corresponding apo-like structures, indicating the importance of considering ligand-bound conformations.

During our screening process, we identified five distinct chemical scaffolds, which we further validated using an LPAR1-dependent calcium flux assay. Although these compounds exhibited weak inhibitory effects, our analysis of 100 ns molecular dynamics simulations provided crucial insights into the structural motifs and interactions involved in the binding process. In our analysis, all residues interacting with the ligands demonstrated low root-mean square fluctuation (RMSF) values, predominantly below 2 Å (Figure S6), which indicated stabilization of these residues. In addition, the RMSD values of the binding sites significantly diminished in the presence of a ligand compared to their apo form (Table S5). Such metrics suggest that ligand binding introduces a stabilizing effect on the system, corroborating the observed activity. It is of particular note that Gln125 emerged as a pivotal residue playing a vital role in protein−ligand interactions. Yet, each compound presented distinct characteristics in their binding process, underlining the multifaceted nature of these interactions. These insights imply that the identified compounds may serve as promising templates or bioisosteres in the design of LPAR1 antagonists.

We also performed calculations for the average binding energy over the course of a 100 ns simulation to investigate its correlation with observed *in vitro* data. When we plotted the average binding energy against percent inhibition, a notable correlation emerged, reflected by an R^2 value of 0.7357 (Figure 8E). Surprisingly, this correlation was absent when comparing the average binding energy with IC_{50} values (Figure 8F). This discrepancy could be due to limitations in the computational models, the complex nature of receptor−ligand interactions, or oversimplifications in our approach that may not capture all aspects of binding dynamics. As noted previously, a study with a larger sample would be essential to make a conclusive statement. Nonetheless, our study demonstrates that the success of the virtual screening process goes beyond the screening methodology alone. Given the complexity of protein−ligand interactions, a multifaceted approach is necessary to effectively identify potential compounds.

https://doi.org/10.1021/acsomega.3c04798
ACS Omega 2023, 8, 40375−40386

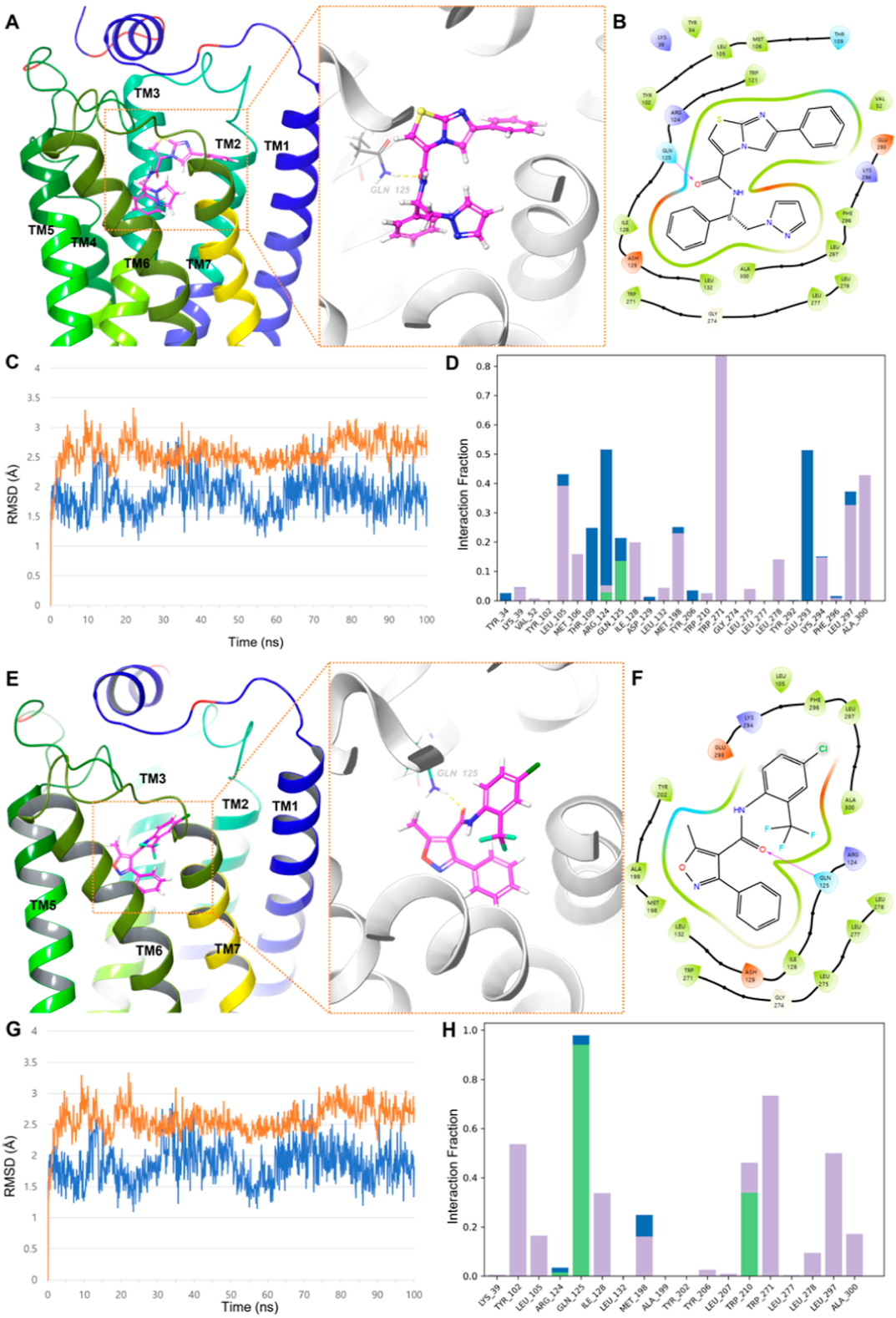

Figure 7. Protein−ligand interaction analysis of compounds 19 and 23. (A,E) Binding pose prediction and (B,F) protein−ligand interaction of compounds 19 and 23, respectively, determined by molecular docking studies. The yellow dashed line indicates hydrogen bonding. (C,G) RMSD plot of protein (orange) and ligand (blue), and (D,H) frequency of interacting residues observed over the course of 100 ns molecular dynamics simulation for compounds 19 and 23, respectively. For the interaction fraction diagram, green indicates hydrogen bonding interactions, purple indicates hydrophobic interactions including $\pi-\pi$ and π−cation interactions, and blue indicates water bridges.

Overall, our study contributes to an improved understanding of protein−ligand interactions in the context of LPAR1 antagonists. We believe that our findings open up new avenues for further exploration and development of novel LPAR1 antagonists.

https://doi.org/10.1021/acsomega.3c04798
ACS Omega 2023, 8, 40375−40386

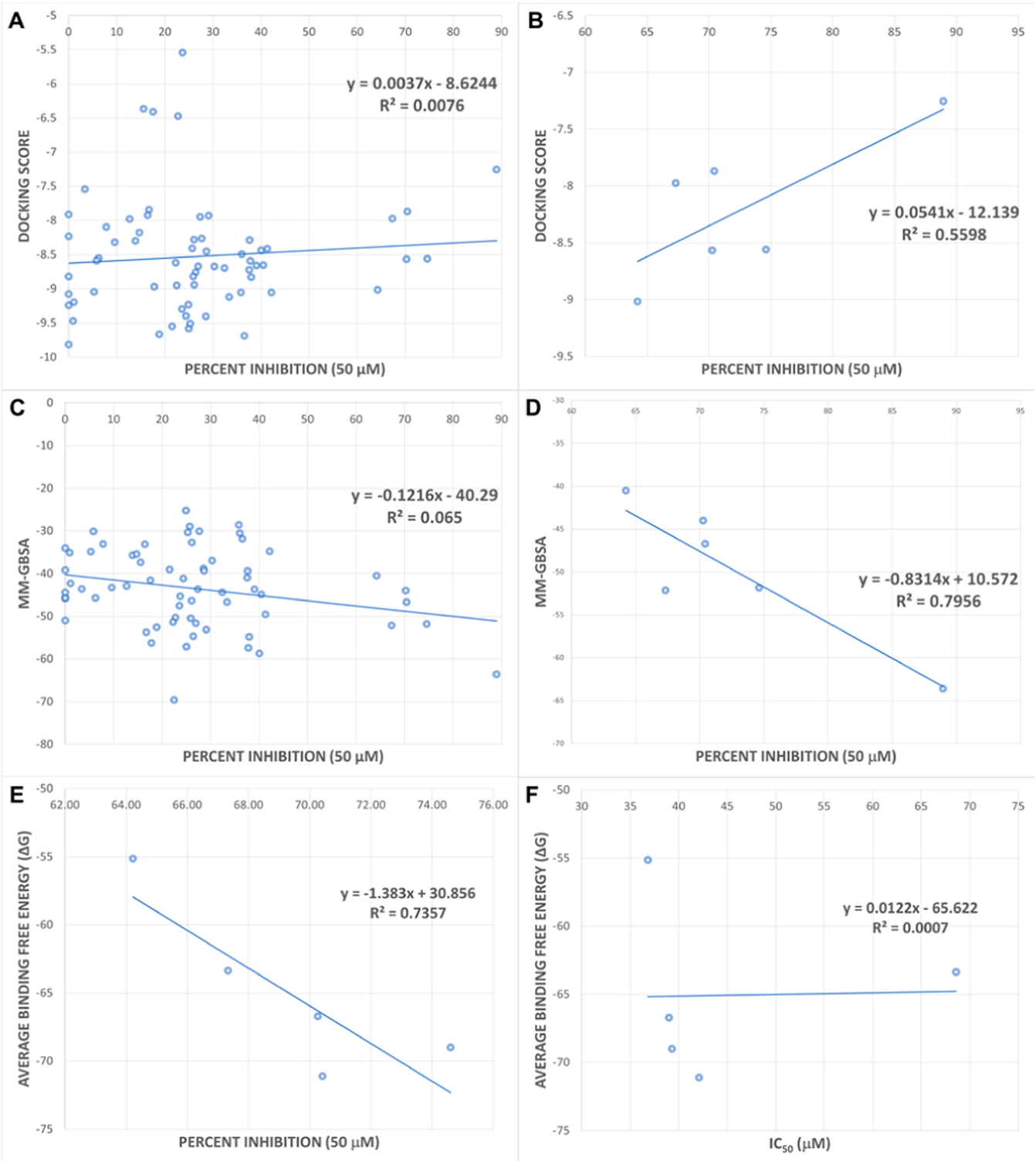

Figure 8. Correlation study of the docking score and MM-GBSA with respect to percent inhibition. Docking score *vs* percent inhibition plot of (A) full 64 compounds tested, and (B) five actives and AM095. MM-GBSA *vs* percent inhibition plot for (C) full 64 compounds and (D) five actives and AM095. Average binding free energy of the five compounds during the course of 100 ns simulation *vs* (E) percent inhibition at 50 μM, and (F) IC_{50} value.

4. MATERIALS AND METHODS

4.1. General Information. All *in silico* experiments, except for molecular dynamics simulation, were performed in a Windows OS environment running on an HP EliteDesk 800 G9 TWR Workstation. Preprocessing for molecular docking (Protein Preparation Wizard, LigPrep, Receptor Grid Generation), virtual screening (Glide), visualization (Maestro), and analysis were conducted with the Schrodinger Small Molecule Drug Discovery Suite (version 2022-4). Molecular dynamics simulation was performed using Desmond on the Schrodinger platform, in a Linux environment on NVIDIA RTX 3080.

https://doi.org/10.1021/acsomega.3c04798
ACS Omega 2023, 8, 40375−40386

4.2. DUD-E Generation. The SMILES of the 10 selected compounds were submitted for DUD-E generation (https://dude.docking.org/).[20] The results were loaded in Microsoft Excel, and the generated forms with charges and their corresponding decoys were removed from the list, resulting in a total of 510 unique SMILES.

4.3. Molecular Docking Experiments. *4.3.1. Protein Preparation.* PDBs (4Z34, 4Z35, 4Z36) and AF-Q92633-F1-model_v4 were loaded onto Maestro, and the proteins were prepared for docking using the Protein Preparation Workflow[28] module. Missing side chains and loops were filled with Prime,[29] and the PROPKA package was used for optimization. Minimization was processed with the OPLS4 force field, and water molecules 5 Å distant from the ligand were removed.

4.3.2. Ligand Preparation. All ligands were prepared using Schrodinger's LigPrep module with the OPLS4 force field. All possible states at a target pH of 7.0 ± 2.0 were generated using Epik,[30] and the only the specified chiralities were retained.

4.3.3. Receptor Grid Generation. For crystal structures, the receptor grid was generated by employing the bound ligand as the centroid for docking. For the AlphaFold model, the binding sites were initially identified using the SiteMap[31] module. The grid was then generated based on the site that corresponds to the region where ligands are bound in crystal structures.

4.3.4. Ligand Docking. Ligands were docked using Glide with varying precision. In all cases, the ligand docking was conducted using a van der Waals radii scaling factor of 0.80 with a partial charge cutoff at 0.15. Ligand sampling was left flexible, and Epik state penalties were applied to the docking scores.

4.3.5. Native Ligand Docking. To test the reliability of the docking protocol, the co-crystallized ligands were docked into their corresponding crystal structures. All three models produced ligand binding poses with an RMSD of less than 1.5 Å with respect to the crystal structure (Figure S7).

4.3.6. Virtual Screening Workflow. The ligands were pre-prepared using the LigPrep function, and therefore, the ligand preparation step was skipped. No filtering was applied in any of the VSW experiments. Epik state penalties were applied to docking scores. For HTVS and SP screening, the top 20% were kept with one pose per compound state. For XP screening, the top 3 compounds were kept.

4.4. Molecular Dynamics Simulation. The system for molecular dynamics simulation was built as an orthorhombic box shape (10 × 10 × 10 Å) employing SPC as the solvent model with an OPLS4 force field. The POPC (300 K) membrane model was applied, and the system was neutralized by adding an appropriate number of counterions. The built system was loaded onto Desmond, and a 100 ns simulation was carried out with *NPT* as the ensemble class running at 300.0 K temperature and 1.01325 bar pressure. The model system was relaxed with the default protocol prior to simulation, and the results were analyzed using Simulation Interactions Diagram (SID).

4.5. Detection of Intracellular Calcium Increase. Changes in intracellular calcium were detected using a new NanoBiT-based method as described previously.[32] In summary, HEK293 cells that stably expressed the human LPA1 receptor were seeded at a density of 2×10^4 cells/well in 96-well plates. The next day, 25 ng of each plasmid including calmodulin tagged with SmBiT at the C-terminal and the binding motif of myosin-light chain kinase 2 tagged with LgBiT at the N-terminal were mixed with 0.06 μL of jetOPTIMUS (Polyplus, Illkirch-Graffenstaden, France) and added to the plated cells. Subsequent steps were performed according to the manufacturer's instructions. After 24 h, the cells were treated with either vehicle (0.2% DMSO) or different compounds at various concentrations and incubated for 20 min at 37 °C, followed by 10 min at room temperature to stabilize the cells before measuring the luminescence. Next, 25 μL of Nano-Glo Live Cell Reagent (furimazine) was added to each well, and the basal luminescence was measured for the first 5 min. Finally, the cells were stimulated by adding 10 μL of LPA at a final concentration of 100 nM to each well, and the real-time change in the luminescence signal was recorded for 15 min.

4.6. Statistical Analysis for IC_{50} Determination. To determine IC_{50} for AM095 and other compounds, a fourfold serial dilution starting from 50 μM and a twofold serial dilution starting from 200 μM were used, respectively. The final percentage of DMSO was less than 0.5%. The relative change in LPA-induced luciferase activity in the presence of the inhibitor was plotted against inhibitor concentration on a logarithmic scale. The IC_{50} and standard deviation (SD) value was calculated through a nonlinear regression analysis [log(inhibitor concentration) *vs* response-variable slope (four parameters)] from three independent experiments using GraphPad Prism 8 software (San Diego, CA, USA). The equation of the curve is given as follows

$$Y = \text{Bottom} + (\text{Top} - \text{Bottom}) / (1 + 10^{((\text{Log } IC_{50} - X)\cdot \text{Hill Slope})})$$

where Y is the fold increase in the luminescence signal; X is the logarithm of the inhibitor concentration; Bottom refers to Y_{min}; and Top refers to Y_{max}.

■ ASSOCIATED CONTENT

Supporting Information

The Supporting Information is available free of charge at https://pubs.acs.org/doi/10.1021/acsomega.3c04798.

Additional experimental details, including complete list of the compounds studied and of the virtual screening campaign, and additional molecular dynamics analysis details (PDF)

■ AUTHOR INFORMATION

Corresponding Authors

Jong-Ik Hwang − *Department of Biomedical Sciences, College of Medicine, Korea University, Seoul 02841, Republic of Korea*; Email: hjibio@korea.ac.kr

Hong-Rae Kim − *Department of Biomedical Sciences, College of Medicine, Korea University, Seoul 02841, Republic of Korea*; orcid.org/0000-0001-5361-7168; Email: hrkim07@korea.ac.kr

Authors

Lan Phuong Nguyen − *Department of Biomedical Sciences, College of Medicine, Korea University, Seoul 02841, Republic of Korea*

Rasel Ahmed Khan − *Department of Biomedical Sciences, College of Medicine, Korea University, Seoul 02841, Republic of Korea*; orcid.org/0000-0003-4911-4335

Soomin Kang − *Department of Biomedical Sciences, College of Medicine, Korea University, Seoul 02841, Republic of Korea*

https://doi.org/10.1021/acsomega.3c04798
ACS Omega 2023, 8, 40375−40386

Hobin Lee − *Department of Biomedical Sciences, College of Medicine, Korea University, Seoul 02841, Republic of Korea*

Complete contact information is available at: https://pubs.acs.org/10.1021/acsomega.3c04798

Author Contributions

L.P.N. conducted the *in vitro* experiments; R.A.K., S.K., and H.L. conducted the *in silico* studies; and H.-R.K. and J.-I.H. designed the study and conducted the analysis. All authors were involved in writing the manuscript.

Notes

The authors declare no competing financial interest.

■ ACKNOWLEDGMENTS

We would like to thank LNP Solution (Republic of Korea) for their invaluable consulting and support on the molecular dynamics study. This work was supported by the National Research Foundation of Korea (NRF) grant funded by the Korea government (MSIT) (RS-2022-00165619).

■ REFERENCES

(1) Okudaira, S.; Yukiura, H.; Aoki, J. Biological roles of lysophosphatidic acid signaling through its production by autotaxin. *Biochimie* **2010**, *92* (6), 698−706.

(2) Geraldo, L. H. M.; Spohr, T. C. L. D.; Amaral, R. F. d.; Fonseca, A. C. C. d.; Garcia, C.; Mendes, F. D.; Freitas, C.; dosSantos, M. F.; Lima, F. R. S. Role of lysophosphatidic acid and its receptors in health and disease: novel therapeutic strategies. *Signal Transduction Targeted Ther.* **2021**, *6* (1), 45.

(3) Xiang, H. J.; Lu, Y. F.; Shao, M. M.; Wu, T. Lysophosphatidic Acid Receptors: Biochemical and Clinical Implications in Different Diseases. *J. Cancer* **2020**, *11* (12), 3519−3535.

(4) Shea, B. S.; Tager, A. M. Role of the lysophospholipid mediators lysophosphatidic acid and sphingosine 1-phosphate in lung fibrosis. *Proc. Am. Thorac. Soc.* **2012**, *9* (3), 102−110.

(5) Ahluwalia, N.; Shea, B. S.; Tager, A. M. New Therapeutic Targets in Idiopathic Pulmonary Fibrosis Aiming to Rein in Runaway Wound-Healing Responses. *Am. J. Respir. Crit. Care Med.* **2014**, *190* (8), 867−878.

(6) Tager, A.; LaCamera, P.; Shea, B.; Campanella, G.; Karimi-Shah, B.; Kim, N.; Zhao, Z.; Polosukhin, V.; Xu, Y.; Blackwell, T.; et al. The lysophosphatidic acid receptor LPA1 links pulmonary fibrosis to lung injury by mediating fibroblast recruitment and vascular leak. *Inflammation Res.* **2007**, *56*, S347.

(7) Swaney, J. S.; Chapman, C.; Correa, L. D.; Stebbins, K. J.; Bundey, R. A.; Prodanovich, P. C.; Fagan, P.; Baccei, C. S.; Santini, A. M.; Hutchinson, J. H.; et al. A novel, orally active LPA(1) receptor antagonist inhibits lung fibrosis in the mouse bleomycin model. *Br. J. Pharmacol.* **2010**, *160* (7), 1699−1713.

(8) Squibb, B. M. Bristol Myers Squibb's Investigational LPA1 Antagonist Reduces the Rate of Lung Function Decline in Patients with Idiopathic Pulmonary Fibrosis. 2023, https://news.bms.com/news/details/2023/Bristol-Myers-Squibbs-Investigational-LPA1-Antagonist-Reduces-the-Rate-of-Lung-Function-Decline-in-Patients-with-Idiopathic-Pulmonary-Fibrosis/default.aspx Accessed on July 5, 2023.

(9) Xiao, D. Q.; Su, X. J.; Gao, H.; Li, X. H.; Qu, Y. The Roles of Lpar1 in Central Nervous System Disorders and Diseases. *Front. Neurosci.* **2021**, *15*, 710473.

(10) Cheng, P. T. W.; Kaltenbach, R. F.; Zhang, H.; Shi, J.; Tao, S. W.; Li, J.; Kennedy, L. J.; Walker, S. J.; Shi, Y.; Wang, Y.; et al. Discovery of an Oxycyclohexyl Acid Lysophosphatidic Acid Receptor 1 (LPA1) Antagonist BMS-986278 for the Treatment of Pulmonary Fibrotic Diseases. *J. Med. Chem.* **2021**, *64* (21), 15549−15581.

(11) Qian, Y. M.; Hamilton, M.; Sidduri, A.; Gabriel, S.; Ren, Y. L.; Peng, R. Q.; Kondru, R.; Narayanan, A.; Truitt, T.; Hamid, R.; et al. Discovery of Highly Selective and Orally Active Lysophosphatidic Acid Receptor-1 Antagonists with Potent Activity on Human Lung Fibroblasts. *J. Med. Chem.* **2012**, *55* (17), 7920−7939.

(12) Ohta, H.; Sato, K.; Murata, N.; Damirin, A.; Malchinkhuu, E.; Kon, J.; Kimura, T.; Tobo, M.; Yamazaki, Y.; Watanabe, T.; et al. Ki16425, a subtype-selective antagonist for EDG-Family lysophosphatidic acid receptors. *Mol. Pharmacol.* **2003**, *64* (4), 994−1005.

(13) Terakado, M.; Suzuki, H.; Hashimura, K.; Tanaka, M.; Ueda, H.; Kohno, H.; Fujimoto, T.; Saga, H.; Nakade, S.; Habashita, H.; et al. Discovery of ONO-7300243 from a Novel Class of Lysophosphatidic Acid Receptor 1 Antagonists: From Hit to Lead. *ACS Med. Chem. Lett.* **2016**, *7* (10), 913−918.

(14) Khanna, D.; Denton, C. P.; Jagerschmidt, A.; Jasson, M.; Distler, O.; Allanore, Y. SAR100842, an Antagonist of Lysophaphatidic Acid Receptor 1, As a Potential Treatment for Patients with Systemic Sclerosis: Results from a Phase 2a Study. *Arthritis Rheumatol.* **2014**, *66*, S387.

(15) Gu, Z. H.; Yan, Y.; Yao, H. Q.; Lin, K. J.; Li, X. Y. Targeting the LPA1 signaling pathway for fibrosis therapy: a patent review (2010-present). *Expert Opin. Ther. Pat.* **2022**, *32* (10), 1097−1122.

(16) Sivaraman, L.; Gill, M.; Nelson, D. M.; Chadwick, K. D. Structure dependence and species sensitivity of in vivo hepatobiliary toxicity with lysophosphatidic acid receptor 1 (LPA(1)) antagonists. *Toxicol. Appl. Pharmacol.* **2022**, *438*, 115846.

(17) Chrencik, J. E.; Roth, C. B.; Terakado, M.; Kurata, H.; Omi, R.; Kihara, Y.; Warshaviak, D.; Nakade, S.; Asmar-Rovira, G.; Mileni, M.; et al. Crystal Structure of Antagonist Bound Human Lysophosphatidic Acid Receptor 1. *Cell* **2015**, *161* (7), 1633−1643.

(18) Guterres, H.; Park, S. J.; Jiang, W.; Im, W. Ligand-Binding-Site Refinement to Generate Reliable Holo Protein Structure Conformations from Apo Structures. *J. Chem. Inf. Model.* **2021**, *61* (1), 535−546.

(19) Scardino, V.; Di Filippo, J. I.; Cavasotto, C. N. How good are AlphaFold models for docking-based virtual screening? *Iscience* **2023**, *26* (1), 105920.

(20) Mysinger, M. M.; Carchia, M.; Irwin, J. J.; Shoichet, B. K. Directory of Useful Decoys, Enhanced (DUD-E): Better Ligands and Decoys for Better Benchmarking. *J. Med. Chem.* **2012**, *55* (14), 6582−6594.

(21) Halgren, T. A.; Murphy, R. B.; Friesner, R. A.; Beard, H. S.; Frye, L. L.; Pollard, W. T.; Banks, J. L. Glide: A new approach for rapid, accurate docking and scoring. 2. Enrichment factors in database screening. *J. Med. Chem.* **2004**, *47* (7), 1750−1759.

(22) Friesner, R. A.; Murphy, R. B.; Repasky, M. P.; Frye, L. L.; Greenwood, J. R.; Halgren, T. A.; Sanschagrin, P. C.; Mainz, D. T. Extra precision glide: Docking and scoring incorporating a model of hydrophobic enclosure for protein-ligand complexes. *J. Med. Chem.* **2006**, *49* (21), 6177−6196.

(23) Truchon, J. F.; Bayly, C. I. Evaluating virtual screening methods: Good and bad metrics for the "early recognition" problem. *J. Chem. Inf. Model.* **2007**, *47* (2), 488−508.

(24) Fresnais, L.; Ballester, P. J. The impact of compound library size on the performance of scoring functions for structure-based virtual screening. *Briefings Bioinf.* **2021**, *22* (3), bbaa095.

(25) Kontoyianni, M. Library size in virtual screening: is it truly a number's game? *Expert Opin. Drug Discovery* **2022**, *17* (11), 1177−1179.

(26) Plewczynski, D.; Lazniewski, M.; Augustyniak, R.; Ginalski, K. Can We Trust Docking Results? Evaluation of Seven Commonly Used Programs on PDBbind Database. *J. Comput. Chem.* **2011**, *32* (4), 742−755.

(27) Wang, Z.; Sun, H. Y.; Yao, X. J.; Li, D.; Xu, L.; Li, Y. Y.; Tian, S.; Hou, T. J. Comprehensive evaluation of ten docking programs on a diverse set of protein-ligand complexes: the prediction accuracy of sampling power and scoring power. *Phys. Chem. Chem. Phys.* **2016**, *18* (18), 12964−12975.

(28) Madhavi Sastry, G.; Adzhigirey, M.; Day, T.; Annabhimoju, R.; Sherman, W. Protein and ligand preparation: parameters, protocols,

and influence on virtual screening enrichments. *J. Comput.-Aided Mol. Des.* **2013**, *27* (3), 221−234.
(29) Jacobson, M. P.; Pincus, D. L.; Rapp, C. S.; Day, T. J. F.; Honig, B.; Shaw, D. E.; Friesner, R. A. A hierarchical approach to all-atom protein loop prediction. *Proteins* **2004**, *55* (2), 351−367.
(30) Shelley, J. C.; Cholleti, A.; Frye, L. L.; Greenwood, J. R.; Timlin, M. R.; Uchimaya, M. Epik: a software program for pK(a) prediction and protonation state generation for drug-like molecules. *J. Comput.-Aided Mol. Des.* **2007**, *21* (12), 681−691.
(31) Halgren, T. New method for fast and accurate binding-site identification and analysis. *Chem. Biol. Drug Des.* **2007**, *69* (2), 146−148.
(32) Nguyen, L. P.; Nguyen, H. T.; Yong, H. J.; Reyes-Alcaraz, A.; Lee, Y. N.; Park, H. K.; Na, Y. H.; Lee, C. S.; Ham, B. J.; Seong, J. Y.; et al. Establishment of a NanoBiT-Based Cytosolic Ca2+ Sensor by Optimizing Calmodulin-Binding Motif and Protein Expression Levels. *Mol. Cells* **2020**, *43* (11), 909−920.

https://doi.org/10.1021/acsomega.3c04798
ACS Omega 2023, 8, 40375−40386